Materials Advances

PAPER

Check for updates

Plasmonic enhancement of photothermal conversion in hydrogels using gold nanorods†

Mai S. Rashwan, [ID] [a] Md. Masud Alam,[a] Seyed Hassan Jaberi, [ID] [b] Abdel-Aziz Al-Sheikh,[a] Anna Cristina S. Samia, [ID] [a] Harihara Baskaran*[b] and Clemens Burda [ID] *[a]

This study investigates the size- and shape-dependent photothermal properties of CTAB-capped gold nanorods (Au NRs) and citrate-capped gold nanospheres (Au NSs) incorporated into hydrogel matrices. Au NRs were synthesized using a modified seed-mediated growth method, resulting in varied sizes and aspect ratios (ARs). Nanoparticles were characterized to ensure uniform optical concentration, enabling a direct comparison between Au NRs and Au NS/hydrogels. By equalizing the optical concentration, we ensured that the hydrogels had the same extinction at 785 nm and 808 nm. Under laser irradiation at these wavelengths, the photothermal conversion efficiency (PCE) of Au NR/hydrogels was found to be comparable to that of Au NS/hydrogels, indicating that differences in the size, shape, and aspect ratio do not significantly impact the overall PCE. Thermal stability tests confirmed the robustness of the plasmonic properties of Au NRs within the hydrogel matrix after heating, further supporting their potential for sustainable and efficient photothermal applications. This work offers insights into the design and optimization of nanomaterial-based systems for photothermal energy conversion, paving the way for advanced applications in biomedical and energy fields.

1. Introduction

Photothermal conversion, the process of converting absorbed light into heat, has garnered significant attention, particularly in biomedical applications and materials science.[1–7] Gold nanomaterials have emerged as versatile platforms for various biological applications, including drug delivery,[8,9] cancer therapy,[10,11] diagnostics,[12–15] radio sensitization,[16] and the induction of cellular hyperthermia.[17–19] The effectiveness of these applications depends on the size, shape, optical properties, and surface functionalization of the nanoparticles making it essential to optimize these characteristics for optimal results.[20–22] Gold nanospheres (Au NSs) exhibit a single surface plasmon resonance (SPR) peak in the visible range, typically around 520–530 nm for particles smaller than 20 nm, with the peak shifting towards the red region of the electromagnetic spectrum as the particle size increases.[20] In contrast, gold nanorods (Au NRs), with their elongated shape, exhibit anisotropic optical properties characterized by two distinct surface plasmon resonance (SPR) peaks: one in the visible range for transverse electron oscillations and another in the near-infrared (NIR) range for longitudinal oscillations.[20,23] This unique dual-peak behavior arises from electron oscillations along the short and long axes of the nanorods, respectively. The longitudinal SPR peak (LSPR) is highly versatile and can be tuned by adjusting the aspect ratio (AR) of the nanorods, enabling shifts across a broad wavelength range (600–1300 nm).[23,24] This tunability stems from the relationship between the AR and the longitudinal plasmon band, where increasing the AR causes a redshift in the peak, while the transverse plasmon band remains relatively constant. The underlying optical principles responsible for these behaviors are well-described by Gans theory,[25] which explains the influence of particle shape and AR on the plasmonic properties of anisotropic nanoparticles. These features make Au NRs valuable for applications requiring precise spectral tuning, such as photothermal therapy and diagnostic imaging.[23,24]

Additionally, Au NRs offer significant flexibility in surface functionalization,[26] enabling customization for targeted applications such as cancer treatment,[10,11] drug delivery,[8,9] and biosensing.[27] These properties make Au NRs particularly suitable for photothermal therapy, where NIR light is ideal for deep tissue penetration and efficient heat generation.[28] When embedded in hydrogels, Au NRs form composite materials with enhanced thermal properties.[17,28] However, the efficiency of

[a] Department of Chemistry, Case Western Reserve University, Cleveland, OH, USA. E-mail: burda@case.edu

[b] Department of Chemical & Biomolecular Engineering, Case Western Reserve University, Cleveland, OH, USA. E-mail: Harihara.Baskaran@case.edu

† Electronic supplementary information (ESI) available. See DOI: https://doi.org/10.1039/d5ma00278h

photothermal conversion depends on the size of the Au NRs and the wavelength of the excitation source,[29] as these factors influence the SPR peak, which governs the nanoparticle's ability to absorb and convert light into heat.

Cetyltrimethylammonium bromide (CTAB) is a positively charged surfactant that is often used as a functional group for Au NRs. It is essential for controlling their rod-like shape and stability. CTAB also controls the nanorods' aspect ratio, which determines their optical properties in the NIR range.[20,27] However, CTAB is known for its cytotoxicity. The positively charged quaternary ammonium headgroup can disrupt cell membranes, leading to cell death.[8,9] Thus, thorough purification is essential to remove excess CTAB, to be further used in biological applications. Replacing CTAB with biocompatible functional groups like polyethylene glycol (PEG) is one way to eliminate cytotoxicity concerns.[28]

The size and AR of Au NRs are crucial factors influencing their photothermal conversion efficiency (PCE), primarily due to their impact on the SPR peak. As the AR increases, the LSPR peak shifts to longer, redshifted wavelengths, enhancing absorption in the NIR region. This characteristic is particularly beneficial for photothermal therapy, as NIR light penetrates biological tissues more effectively, enabling deeper tissue heating.[30,31] Domingo-Diez et al.[32] showed that Au NRs capped with cetyltrimethylammonium bromide (CTAB), with dimensions of 68 ± 4 nm in length and 20 ± 2 nm in diameter, exhibit efficient light-to-heat conversion upon irradiation with an 808 nm laser. These Au NRs, dispersed in Dulbecco's modified Eagle medium (DMEM) without phenol red, demonstrate increased tissue penetration and higher localized temperatures as their concentration increases. Zhou et al.[33] explored the PTT effect of Au NRs with aspect ratios of 3.3, 3.5, 4.1, and 5.4, lengths of 68 nm and 40 nm and diameters of 20 nm and 10 nm, respectively, taken by HepG2 cells upon applying a femtosecond pulse laser, aiming for cytotoxicity, which also proved effective upon excitation with the same 808 nm laser wavelength. These Au NRs exhibited more uniform heating profiles and faster heating dynamics, with different laser wavelengths used for each AR.[33] In both studies, the average AR of these Au NRs was approximately 3.3, highlighting the importance of AR in optimizing photothermal conversion efficiency for therapeutic applications. Diallo et al.[34] evaluated the effect of size, shape and excitation wavelength on the photothermal heat generation of gold nanourchins and Au NRs by measuring their absorption coefficients. Their results demonstrated that NRs, when excited near their LSPR, exhibited better photothermal performance compared to nanourchins.[34] Amarasekara et al.[35] developed temperature-responsive Au NSs by functionalizing citrate-capped Au NSs with elastin-like polypeptides, achieving tunable agglomeration reaching a temperature range of 34–50 °C, and enhanced photothermal efficiency up to 68%, under NIR irradiation.[35] These studies demonstrate antibiofilm activity.

Our work on the photothermal conversion efficiency of Au NSs in agarose hydrogels investigated the effects of nanoparticle size within a low concentration range ($<1\%$ v/v) on thermal response.[36] We demonstrated that larger Au NSs (48 nm) exhibit superior PCE compared to smaller ones. This enhancement is primarily due to stronger plasmonic absorption and Mie scattering within the hydrogel network. This was confirmed by extinction measurements. While Au NS incorporation strongly enhanced photothermal heating, it did not significantly alter the hydrogel's thermal conductivity. These findings highlight the critical role of nanoparticle size in optimizing photothermal performance for biomedical and photothermal applications.

The laser wavelength plays a critical role in the photothermal heating of nanomaterials, influencing the efficiency of heat generation.[37] For Au NRs and Au NSs, the excitation wavelength should be closely matched with the particle's LSPR to achieve optimal PCE.[38] The 808 nm wavelength is widely used due to its favorable alignment with the LSPR of many Au NRs, especially those with an AR ranging from 2 to 4, providing effective energy absorption and deeper tissue penetration.[39–42] However, this wavelength may cause unwanted heating in surface-targeted applications.[43] In contrast, the 785 nm wavelength is preferred for its lower penetration depth, which is advantageous for more localized heating, particularly in Au NSs with an SPR around 520 nm.[44] While 808 nm and 785 nm are close in wavelength, both have distinct roles in medicinal phototherapy. Ultimately, the choice of wavelength depends on the nanoparticle type and the specific application requirements.

The size of the Au NRs also plays a crucial role in thermal dissipation. Smaller NRs tend to have higher surface-to-volume ratios, which can lead to faster thermal dissipation, thus affecting their heating efficiency.[45] On the other hand, larger Au NRs experience enhanced Mie scattering effects, which can overshadow their absorption capabilities.[33,46] However, in our study on ND hydrogels,[47] increased scattering was found to be beneficial, as it enhanced the overall photothermal performance.

In this paper, we compare the PCE of Au NRs with varying sizes and ARs with Au NSs, each dispersed in separate agarose gel matrices upon irradiation with two different wavelength (785 and 808 nm) laser sources. This setup improves the dispersibility of the particles while preventing stability issues.[48] Agarose gel serves as an ideal model for mimicking brain tissue due to its similarity in the dynamic mechanical properties.[49] Additionally, the non-toxicity of agarose makes it suitable for a broad range of industrial and biological applications.[50–53] The concentrations of Au NRs with varying ARs and Au NSs dispersed in the gel were adjusted using UV-vis spectroscopy to achieve equal optical extinction. This approach standardizes the initial optical conditions of the hydrogels, enabling a leveled comparison of PCE and heat transfer performance across the different nanoparticle types. The optical equalization ensures that any observed differences in photothermal behavior are attributed solely to particle shape, size, and optical properties rather than discrepancies in the number of photons absorbed (extinction).

2. Experimental

2.1. Materials

Chemicals and materials: cetyltrimethylammonium bromide (CTAB, 99%), gold(III) chloride (HAuCl$_4$, 30 wt% in dilute HCl),

silver nitrate (99%), sodium borohydride (98%), and ascorbic acid (99%) were purchased from Sigma-Aldrich (Burlington, MA). Sodium oleate (97%) was obtained from TCI America, sodium citrate from Fisher Scientific, and agarose from Thermo Fisher Scientific.

2.2. Synthesis of Au NRs and Au NSs

2.2.1. Synthesis of Au NSs. Citrate-capped gold nanospheres (Au NSs) were synthesized using the classical Turkevich method.[54] A volume of 66.6 μL of 30 wt% $HAuCl_4$ solution was added to 125 mL of deionized water preheated to 95 °C. The solution was stirred for 3 minutes, followed by the dropwise addition of 10 mL of 0.1 M sodium citrate under vigorous stirring. The reaction mixture was maintained at 95 °C for approximately 6 minutes, with the container covered by a Petri dish to minimize contamination and solvent evaporation. The formation of a stable wine-red color indicated the successful synthesis of the nanoparticles. The solution was then allowed to cool to room temperature.

2.2.2. Synthesis of Au NRs. Au NRs were synthesized using a seed-mediated, surfactant-assisted growth method.[55,56] The seed solution was prepared by mixing 1 mL of 2.5 mM $HAuCl_4$ with 9 mL of 0.1 M CTAB in water. Reduction was initiated by adding 210 μL of 0.01 M $NaBH_4$ dropwise, causing the solution to change from yellow to reddish-brown. The mixture was stirred for 2 minutes, and the resulting seed solution was stored in the dark at room temperature for at least 2 hours before use.

To prepare the growth solution for extra-small Au NRs, 0.89 g of CTAB and 0.135 g of sodium oleate were dissolved in 25 mL of warm water (~50 °C). After adding 1.5 mL of 3.89 mM $AgNO_3$ dropwise, the solution was briefly stirred for 10 seconds at 700 rpm and left undisturbed for 15 minutes. Then, 25 mL of 1 mM $HAuCl_4$ was added and stirred at 700 rpm for 1 hour. The pH was adjusted to 4 by adding 160 μL of 12 M HCl. The reduction of Au(ı) to Au(0) was achieved by adding 125 μL of 0.074 M ascorbic acid, followed by 30 seconds of stirring. Finally, 25 μL of the seed solution was added while stirring at 1200 rpm for 30 seconds.

Short, medium, and long Au NRs were synthesized by varying the amounts of CTAB, sodium oleate, silver nitrate, and HCl. For short Au NRs, 0.95 g of CTAB, 0.135 g of sodium oleate, 1.8 mL of 4 mM $AgNO_3$, and 160 μL of 12 M HCl were used. For medium Au NRs, 0.99 g of CTAB, 1.9 mL of 4 mM $AgNO_3$, and 175 μL of 12 M HCl were used. For large Au NRs, 1.10 g of CTAB, 2.2 mL of 4 mM $AgNO_3$, and 200 μL of 12 M HCl were used. In each case, ascorbic acid (0.064–0.074 M) and the seed solution were added with stirring.

After synthesis, the Au NR solutions were left undisturbed overnight, followed by centrifugation at 7000 rpm for 20 minutes. The resulting precipitate was re-dispersed in 5 mL of deionized water for further use.

To monitor the LSPR peak of Au NRs and the SPR peak of Au NSs, absorption spectra were collected using UV-visible spectroscopy. The Au NSs, with a diameter of 17 nm, exhibit an SPR peak at 520 nm. For the Au NR samples, extra short Au NRs show an LSPR peak at 735 nm, reflecting their smaller dimensions. Short Au NRs have a peak at 820 nm, indicative of their intermediate size, while medium Au NRs have a peak at 860 nm. Long Au NRs, with the largest dimensions, have a peak at 934 nm. These results demonstrate that as the particle size and aspect ratio increase, the absorbance peak shifts towards the near-infrared region. The total gold Au concentration in the Au NR samples was measured using an atomic absorption spectrophotometer (AAS). For analysis, 100 μL of the Au NR sample was digested overnight in aqua regia (HNO_3 : HCl, 1:3 molar ratio) to ensure complete dissolution. The digested solution was then diluted to 10 mL with HPLC-grade water before measurement. The liquid sample was introduced into a flame atomizer, where Au^{3+} were reduced to neutral atoms. A gold-specific hollow cathode lamp (HCL) emitting light at 242.8 nm was used as the excitation source. The extent of absorption at this wavelength was recorded, as it is directly proportional to the Au concentration in the sample. A calibration curve was constructed using Au standard solutions (0, 5, 10, 15, 20, 25, 30, and 35 ppm), and the absorbance of the unknown Au NR sample was compared to that obtained using this curve to determine the total gold concentration, expressed in ppm.

2.2.3. Preparation of Au NS and Au NR hydrogels. Au NS/ hydrogels were synthesized using our previously developed method.[36,47] Precise volumes of 17 nm Au NSs and Au NRs (ARs: 2.63, 3.31, 3.6, and 5.5) were introduced into a 2 wt% agarose powder. The mixtures were heated to 80 °C while being stirred to ensure complete dissolution of the agarose and uniform dispersion of the Au NSs and Au NRs. Afterward, the hydrogels were poured into a custom-designed 3D-printed container and allowed to cool to room temperature. To facilitate temperature monitoring for heat transfer measurements, eight thermocouples were inserted through predefined holes in the container lid. A 2 wt% agarose gel was selected for this study to ensure adequate stability, as lower concentrations resulted in insufficient firmness, whereas higher concentrations created excessive rigidity that hindered the ideal experimental setup.[36,47]

3. Results and discussion

3.1. Results

3.1.1. Characterization of different Au NP shapes. CTAB-capped Au NRs were synthesized using a modified seed-mediated, surfactant-assisted growth method,[55–57] enabling the production of four distinct sizes and aspect ratios (ARs). Citrate-capped Au NSs were synthesized using the classical Turkevich method.[54] TEM analysis, shown in Fig. 1, confirmed the precise control over Au NR dimensions. The extra-short Au NRs (Fig. 1a) had dimensions of 102.3 ± 1.6 nm in length (L) and 43.9 ± 1.3 nm in width (W), corresponding to an AR of 2.63. The short Au NRs (Fig. 1b) measured 110.2 ± 1.6 nm (L) and 33.2 ± 1.8 nm (W), with an AR of 3.31. The medium Au NRs (Fig. 1c) had dimensions of 123.5 ± 2.7 nm (L) and
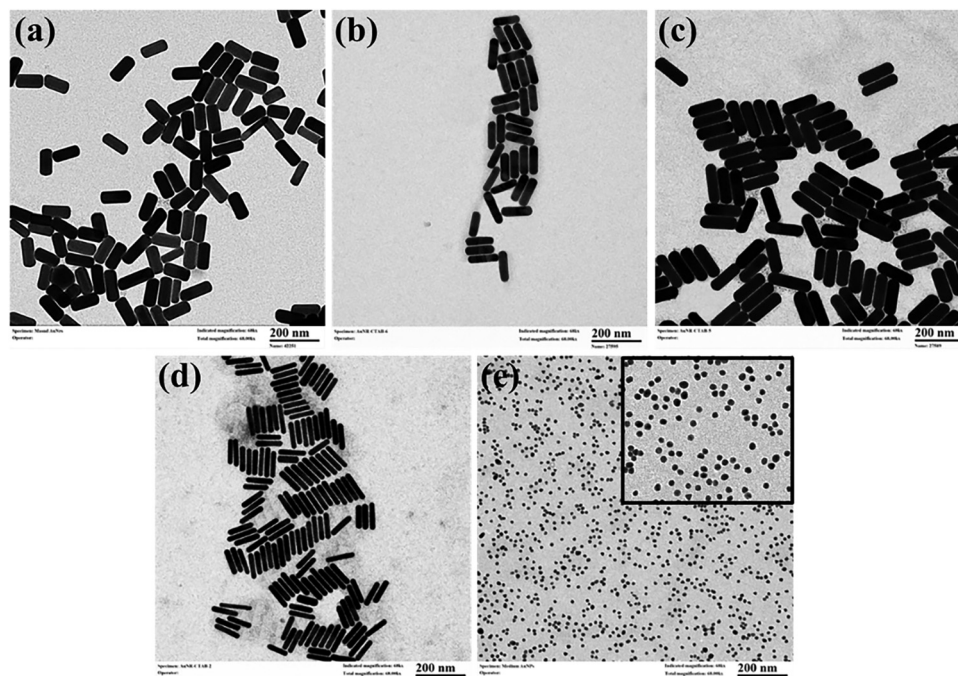
Fig. 1 TEM images of CTAB-coated Au NRs with varying sizes and aspect ratios: (a) extra short (102.3 ± 1.6 nm (*L*); 43.9 ± 1.3 (*W*); AR: 2.63), (b) short (110.2 ± 1.6 nm (*L*); 33.2 ± 1.8 (*W*); AR: 3.31), (c) medium (123.5 ± 2.7 nm (*L*); 33.7 ± 2.6 nm (*W*); AR: 3.6), and (d) long (127.4 ± 3.0 nm (*L*); 23.0 ± 4.1 nm (*W*); AR: 5.5). (e) Au NSs with 14 ± 0.5 nm core size, with a zoomed inset image confirming the spherical morphology of the prepared nanoparticles. Scale bars represent 200 nm. The nanorods have a consistent, rod-like shape with little variation in size across the samples.

33.7 ± 2.6 nm (*W*), resulting in an AR of 3.6. Finally, the long Au NRs (Fig. 1d) exhibited the highest AR of 5.5, with dimensions of 127.4 ± 3.0 nm (*L*) and 23.0 ± 4.1 nm (*W*). Additionally, TEM analysis of Au NSs (Fig. 1e) showed a consistent core size of 14 ± 0.5 nm. Dynamic light scattering (DLS) measurements of the Au NSs indicated a hydrodynamic radius of 17 ± 0.2 nm (Fig. S1(a) in the ESI†). DLS measurements of the mean hydrodynamic diameters for the four sizes of Au NRs are shown in Fig. S1(b) in the ESI.† These measurements indicate the successful synthesis of nanorods and nanospheres with systematically varied shapes and sizes, essential for tailoring their optoelectronic properties. Table 1 summarizes the dimensions measured by the TEM, AR, volume, surface area, and wavelength of the absorption peaks of the nanoparticles under study.

3.1.2. UV-visible absorption of Au NS and Au NR solutions. UV-visible absorption spectroscopy provided further insights into the optical properties of the synthesized nanoparticles. Fig. 2(a) illustrates the spectrum of Au NS solution, which exhibits a characteristic SPR peak at 520 nm, indicative of its

isotropic shape and small core size. Fig. 2(b) shows the absorption spectra of the four Au NR solutions with varying ARs. It shows a clear size- and AR-dependent shift in the LSPR peak position. The extra-short Au NRs exhibited an LSPR peak at 735 nm, reflecting their relatively smaller AR. The short Au NRs displayed a peak at 820 nm, the medium Au NRs at 860 nm, and the long Au NRs, with the highest AR, exhibited the most significant redshift, peaking at 934 nm.

3.1.3. Optical extinction equalization for Au NSs and Au NRs in hydrogel matrices. The photothermal energy conversion of 2 wt% agarose gel loaded with Au NSs and Au NRs was investigated. Nanoparticle-loaded hydrogels were prepared following our previously reported protocol.[47] The matrix immobilizes nanoparticles by entrapping them within the porous structure of the galactopyranosyl residues in the agarose network.[58] To ensure a fair comparison between Au NSs and Au NRs, nanoparticle-loaded hydrogels were prepared, and their extinctions were equalized by adjusting their concentrations. This method standardized the experimental conditions by equalizing the optical extinctions of Au NSs/hydrogel and Au

Table 1 Dimensions and optical absorption of five different gold nanoparticle shapes used in this study. 17 nm Au NSs, extra short, short, medium, and long Au NRs

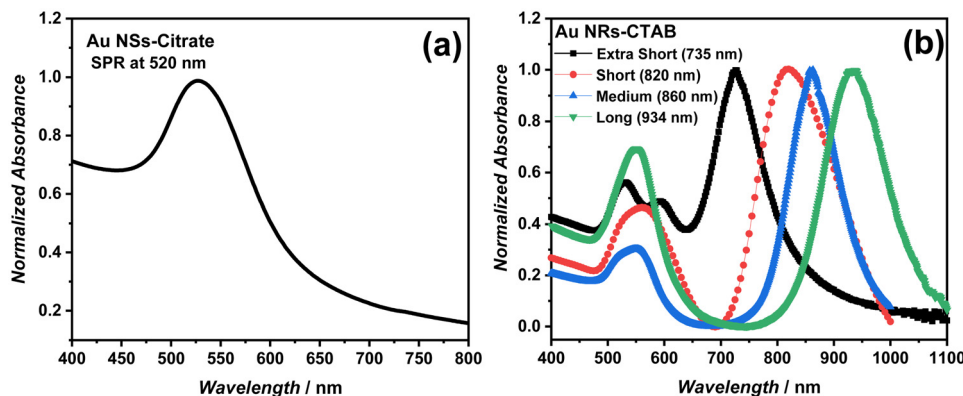| Au NP/property	Length/nm	Width/nm	Aspect ratio (AR)	Volume/nm³	Surface area/nm²	Peak absorption λ/nm
NSs	17 ± 0.5	17 ± 0.5	1	1436.8	615.8	520
E. short NRs	102.3 ± 1.6	43.9 ± 1.3	2.63	154 844.1	17 136.0	735
Short NRs	110.2 ± 1.6	33.2 ± 1.8	3.31	95 399.8	13 225.3	820
Medium NRs	123.5 ± 2.7	33.7 ± 2.6	3.6	110 158.1	14 859.1	860
Long NRs	127.4 ± 3.0	23.0 ± 4.1	5.5	52 931.6	10 036.4	934

Fig. 2 Normalized absorbance spectra of (a) Au NS solution with an SPR peak at 520 nm, (b) Au NR solutions with varying sizes: extra-short (735 nm, black), short (820 nm, red), medium (860 nm, blue), and long (934 nm, green). The spectra are normalized to the absorbance maximum for each sample. These results highlight the variation in the LSPR peak positions as the size of the nanorods increases, with a clear red shift observed for larger sizes.

NR/hydrogels to achieve identical absorption values of 0.61 at both 785 nm and 808 nm as shown in Fig. 3, and the whole spectrum is provided in Fig. 3(a). The prepared hydrogels were subsequently utilized in heat transfer measurements.

3.1.4. Heat transfer measurements of Au NS and Au NR hydrogels under laser irradiation. Heat transfer measurements were conducted for hydrogels containing four different sizes of Au NR and Au NS hydrogels. The hydrogels were irradiated using two distinct laser wavelengths (785 nm and 808 nm) to evaluate the influence of excitation wavelength on the photothermal conversion behavior.

The induced temperature changes after 15 minutes of irradiation at 785 nm are presented in Fig. 4 as a function of the nanoparticles' AR. The results demonstrate that despite variations in the nanoparticle morphology, the temperature changes observed for the different shapes were comparable. Notably, Au NSs and extra short Au NRs (AR = 2.63) exhibited the highest temperature increase relative to plain agarose gel across all monitored locations (Fig. S2 and Table S1 of the ESI†). However, as the AR of Au NRs increased, the temperature

increase leveled off. For extra short Au NRs, the temperature change at a 5 mm distance from the heating spot reached 17.7 °C as shown in Fig. 4(a), while at 15 mm, the temperature increase was 9.7 °C, as shown in Fig. 4(b). For Au NSs, the temperature change at 5 mm was 18.4 °C, as shown in Fig. 4(a), while at 15 mm, the temperature increase reached 8.6 °C, as shown in Fig. 4(b). This spectral proximity likely enhances the PCE, resulting in a slightly greater heat generation compared to other nanoparticle sizes. Extinction was equalized to 0.61 to study effects beyond absorption peaks.

When an 808 nm laser excitation source was used, the highest temperature changes were observed in short Au NRs (AR = 3.31), with their LSPR peak at 820 nm, as shown in Fig. 5. The temperature change at a 5 mm distance from the heating spot reached 11.9 °C as shown in Fig. 5(a), while at 15 mm, the temperature increase was 5.7 °C, as shown in Fig. 5(b). For Au NSs, the temperature change at 5 mm was 16 °C, as shown in Fig. 5(a), while at 15 mm, the temperature increase reached 9 °C, as shown in Fig. 5(b). Despite the difference in the plasmon peaks between the Au NSs and Au NRs, Au NSs
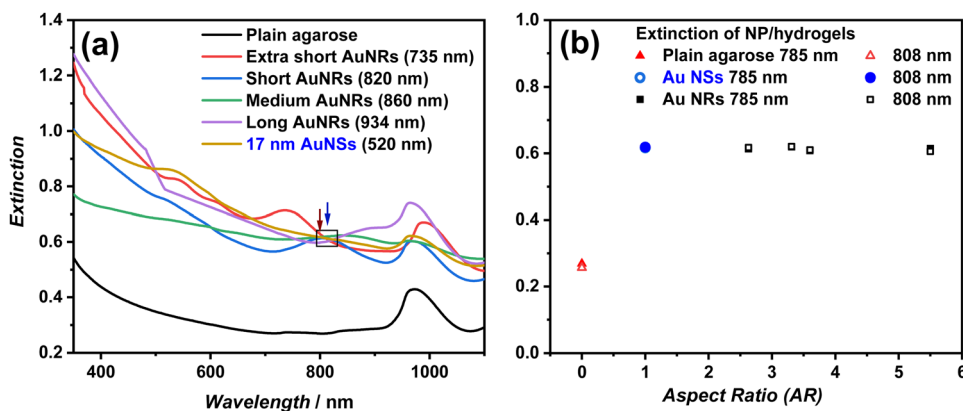

Fig. 3 Optimization of extinction values for 17 nm Au NSs and Au NRs with varying ARs in hydrogels, compared to plain agarose, using an optical concentration calibration approach at 785 and 808 nm. (a) Absorption spectra of NP-laden hydrogels, calibrated to equal extinction at both wavelengths (785 nm, red arrow and 808 nm, blue arrow). (b) Extinction values as a function of AR, ensuring uniform extinction (~0.61) at 785 and 808 nm, enabling direct comparison of photothermal effects independent of absorption variations.
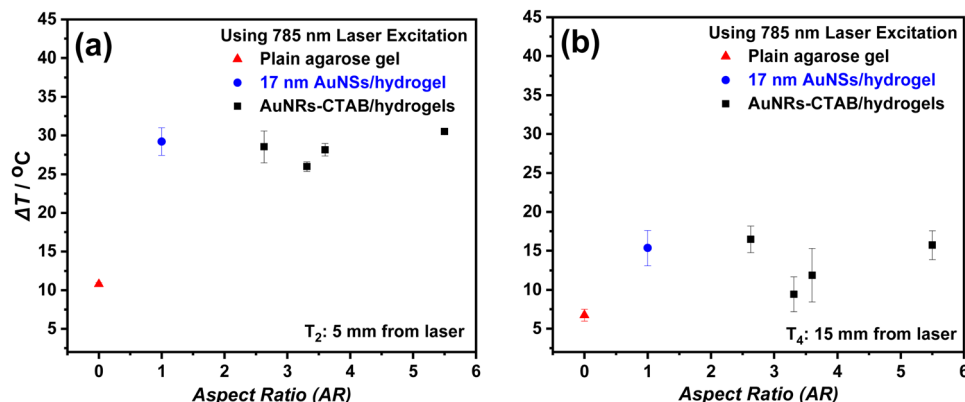
Fig. 4 Temperature changes measured after 15 minute heating under 785 nm laser exposure for plain agarose (red triangles), Au NSs/hydrogel (17 nm, blue circles), and Au NR/hydrogels with varying aspect ratios (black squares) at (a) 5 mm and (b) 15 mm distance from the heating spot (N = 3). The data illustrate the impact of particle shape and size on heat transfer and thermal responses. Symbols represent mean values, and vertical bars indicate standard deviations.
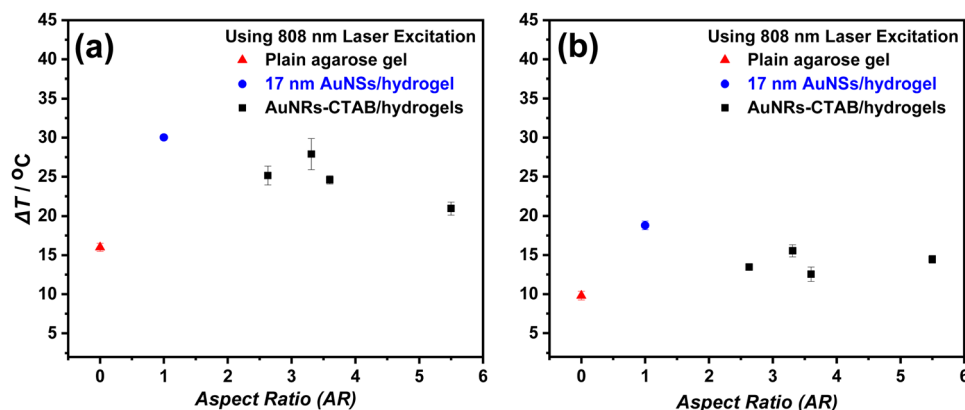

Fig. 5 Temperature changes measured after 15 minute heating under 808 nm laser exposure for plain agarose (red triangles), Au NSs/hydrogel (17 nm, blue circles), and Au NR/hydrogels with varying aspect ratios (black squares) at (a) 5 mm and (b) 15 mm distance from the heating spot (N = 3). The data illustrate the impact of the particle size and shape on heat transfer and thermal responses. Symbols represent mean values, and vertical bars indicate standard deviations.

exhibited a comparable temperature increase with Au NR hydrogels. Heat transfer profiles at all locations within the hydrogels are shown in Fig. S4 and Table S2 in the ESI.†

3.1.5. Thermal stability of LSPR and TSPR peaks in Au NR/ hydrogels. To evaluate the thermal stability of the LSPR and transverse surface plasmon resonance (TSPR) peaks, the extinction spectra of Au NR/hydrogels were measured under various heating conditions. The spectra were recorded under three distinct conditions: no heating (blue spectra), at the heating spot (black spectra), and away from the heating spot (red spectra) as shown in Fig. 6. The four different sizes of Au NRs under study were examined. This indicates that the nanorods' optical properties and plasmonic resonance remained stable even after heating.

3.1.6. Thermal conductivity measurements of Au NS and Au NR hydrogels. Thermal conductivity (TC) measurements for the various shapes and sizes of Au/hydrogels were performed using the transient hot wire technique (THW), as illustrated in

Fig. 7. The plain agarose gel exhibited the lowest TC values, consistent with previous reports indicating that the TC of agarose decreases with increasing concentration.[59,60] Incorporating Au NSs or Au NRs of varying sizes into the hydrogel matrix did not significantly alter the TC values.

3.1.7. Simulated photothermal conversion efficiency of Au NS and Au NR hydrogels. Heat transfer simulations were computed using finite element modeling (COMSOL Multiphysics 6.1, Burlington, MA) for nanoparticle-laden hydrogels to evaluate the significance of minor variations in TC. A literature-reported expression was applied to simulate TC changes.[61] Simulation results indicated that gel heating was minimally influenced by small variations in TC (data not shown).

The effective laser power transferred to the sample was calculated by aligning the modeling results with experimental data. PCE in hydrogels loaded with Au NSs and Au NRs was estimated using experimental observations and computational modeling. Laser power inputs were used to model the
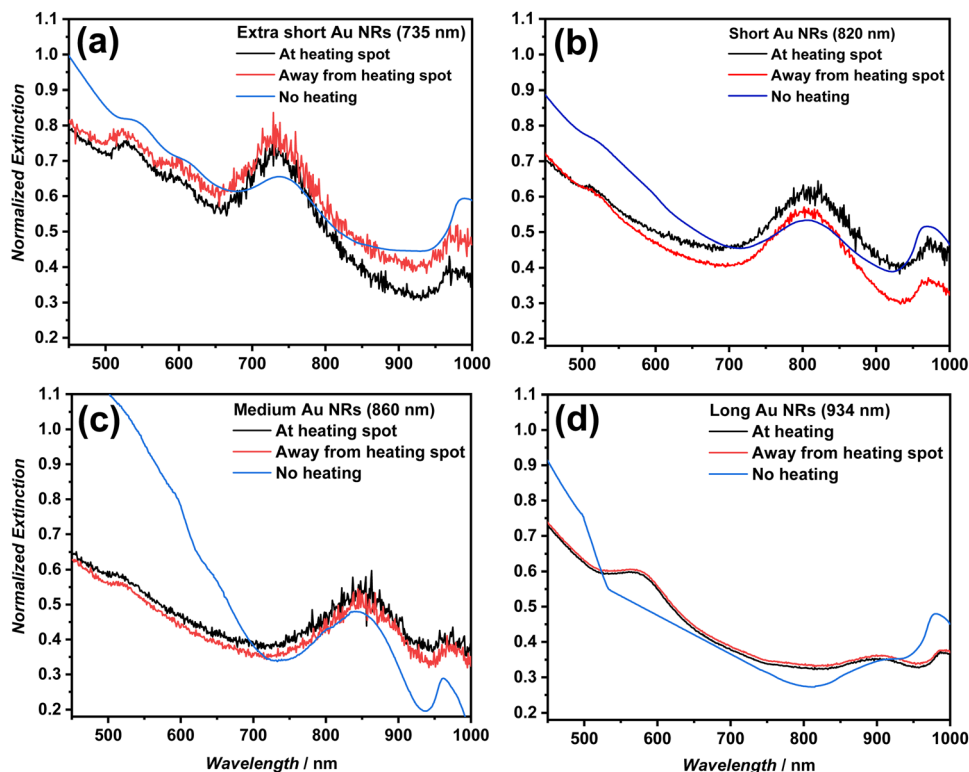
Fig. 6   Extinction spectra of Au NR/hydrogels under localized heating with 785 nm laser excitation for 15 min. (a) Extra short Au NRs with LSPR at 735 nm, (b) short Au NRs with LSPR at 820 nm, (c) medium Au NRs with LSPR at 860 nm, and (d) long Au NRs with LSPR at 934 nm. Spectra were recorded under three conditions: no heating (blue), at the heating spot (black), and away from the heating spot (red). The LSPR and TSPR peaks remain unchanged across all heating conditions, demonstrating the thermal stability of the nanorods embedded in the hydrogel matrix.
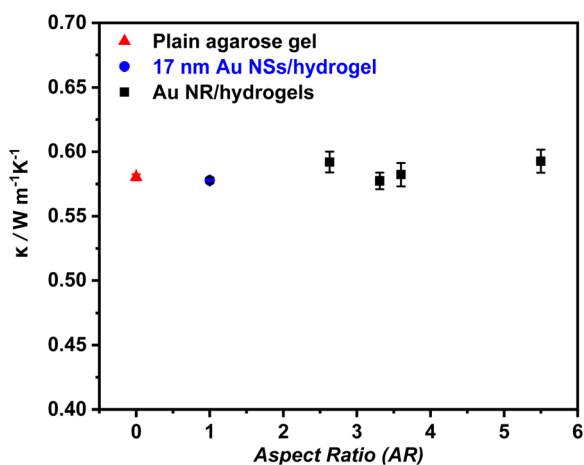

Fig. 7   Thermal conductivity measurements of Au NSs/hydrogel (17 nm, blue circles) and Au NR/hydrogels (black squares) as a function of aspect ratio compared with those of plain agarose gel (red triangle). Thermal conductivity remains nearly constant with increasing aspect ratio for all samples, indicating a negligible impact of nanoparticle incorporation on the hydrogel matrix ($N = 10$). Symbols represent mean values, and vertical bars indicate standard deviations.

temperature distribution inside the gel, incorporating key parameters such as laser intensity, material properties, and sample geometry. This comprehensive computational approach provided precise estimations of PCE and deepened the understanding of the hydrogel's ability to convert incident laser energy into heat.

The PCE values of the nanoparticles studied under 785 nm and 808 nm laser excitation are shown in Fig. 8, as a function of AR, with 95% confidence intervals represented by error bars. At 785 nm (Fig. 8(a)), the PCE of Au NSs was comparable to that of Au NRs. However, Au NRs with an AR of 2.63 (extra short) exhibited the highest PCE, as their LSPR peak at 735 nm is well-matched with the 785 nm excitation. In contrast, at 808 nm (Fig. 8(b)), the PCE of Au NSs was slightly higher than that of the Au NRs, with the Au NRs exhibiting the highest efficiency at an AR of 3.31 (short), as the LSPR peak of this nanorod is at 820 nm, close to this excitation wavelength. Photothermal conversion efficiency values for all Au NP/hydrogels under study are provided in Tables S3 and S4, in the ESI.† Plain agarose gel showed minimal PCE upon using both wavelengths due to the absence of plasmonic properties. The simulation results exhibit strong alignment with our experimental findings, as evidenced by the fitted temperature profiles presented in Fig. S6 and S7, in the ESI.†

3.2.   Discussion

This study investigated the photothermal properties of gold nanoparticles (Au NSs and Au NRs) incorporated into agarose
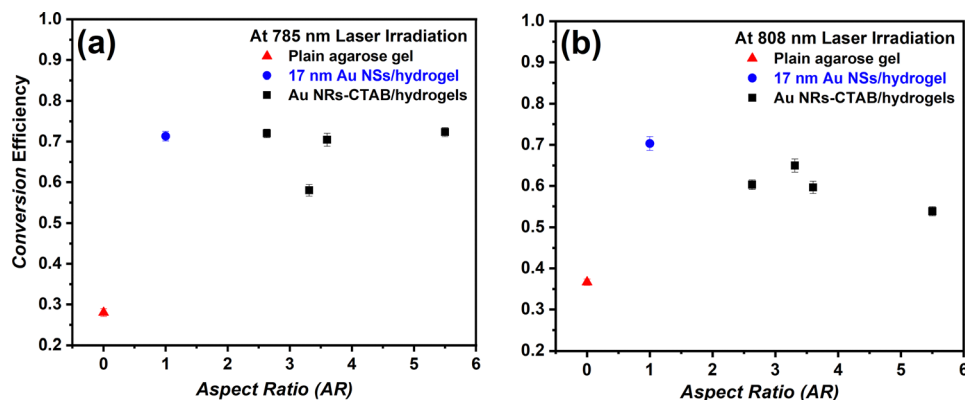
Fig. 8 Photothermal conversion efficiencies as a function of AR using (a) 785 nm and (b) 808 nm laser excitation wavelength. Symbols represent the mean value, and vertical bars indicate the standard deviation.

hydrogels, focusing on the effects of nanoparticle size, shape, and laser wavelength on photothermal energy conversion efficiency (PCE). TEM analysis (Fig. 1) revealed aspect ratios (ARs) ranging from 2.63 to 5.5, influencing the nanoparticles' optical and photothermal behavior. UV-vis absorption spectra (Fig. 2) showed a characteristic SPR peak at 520 nm for Au NSs, shown in Fig. 2(a), while a redshift in the LSPR peak of Au NRs was observed with increasing AR, shown in Fig. 2(b). The combined analysis of Au NS and Au NR solutions emphasizes the versatility of tuning the optical properties through precise control of the nanoparticle size and shape. This ability to fine-tune optical characteristics enables their application in wavelength-specific technologies, such as photothermal energy conversion, biosensing, and other optoelectronic applications, underscoring their potential for tailored technological advancements.

To ensure standardized experimental conditions, the optical extinctions of Au NSs and Au NRs-loaded hydrogels were equalized to ensure standardized experimental conditions (Fig. 3). By adjusting the nanoparticle concentrations to achieve identical extinction values of approximately 0.61 at both 785 nm and 808 nm wavelengths demonstrated in Fig. 3(b), we minimized any discrepancies between the two nanoparticle types. This calibration ensured that variations in photothermal energy conversion efficiencies were due solely to the properties of the nanoparticles.

Heat transfer measurements (Fig. 4 and 5) of the optically equalized hydrogels revealed a minimal impact of the nanoparticle size and shape on the temperature increase. The highest temperature increase occurred for extra-short Au NRs (AR = 2.63) and Au NSs under 785 nm laser irradiation, as presented in Fig. 4(a) at a 5 mm and Fig. 4(b) at a 15 mm distance from the heating spot. This slightly enhanced response is likely due to the closer alignment of the LSPR peak of extra short Au NRs (approximately 735 nm) with the 785 nm excitation wavelength. However, as the AR of Au NRs increased, the temperature increase plateaued. Similarly, the temperature increase was consistent across both nanoparticle types under 808 nm laser irradiation as outlined in Fig. 5(a) and (b) with a slight increase for the short Au NRs (AR = 3.31) whose LSPR

peak is near 820 nm that is close from this excitation wavelength. This suggests that the slight variation in excitation wavelength, nanoparticle shape, and size had a minimal impact on the PCE, suggesting that factors beyond nanoparticle morphology and excitation wavelength influence the photothermal performance. Consistent with the trends observed in Fig. 4 and 5 for the aspect ratio, additional analysis in Fig. S3, S5, and S8 in the ESI† further confirms that the nanoparticle surface area, volume, and SA/V ratio do not significantly influence the photothermal heating behavior or the photothermal conversion efficiency (η) under both 785 nm and 808 nm laser exposure.

Thermal stability measurements observed in Fig. 6(a–d) demonstrated that the LSPR and TSPR peaks of the Au NRs embedded in hydrogels remained stable under various heating conditions, indicating the preservation of their plasmonic properties even under moderate heating. The LSPR peak, which corresponds to collective oscillations of conduction electrons in Au NRs, is highly sensitive to changes in size, shape, and the local environment of the nanoparticles.[62] However, our data suggest that Au NRs maintain their plasmonic resonance within the hydrogel matrix, likely due to their inherent structural stability and the hydrogel's ability to act as a thermal buffer. By limiting drastic temperature fluctuations, the hydrogel prevents overheating and aggregation, preserving the plasmonic properties of the NRs and preventing degradation of their optical behavior.

Similar to the LSPR, the TSPR peaks also exhibit no significant shift or diminishing with heating. The TSPR peak, which is more sensitive to changes in the NS shape or AR, could be expected to shift with temperature-induced changes. The observed stability of both the LSPR and TSPR peaks under the heating conditions suggests that Au NRs retain their structural integrity, and the matrix prevents any significant morphological alterations that might affect the plasmonic properties. This stability suggests that the size-dependent properties of NRs, such as their optical behavior, are robust against moderate thermal fluctuations. This indicates that the applied temperature range does not significantly impact the electronic structure or morphology of Au NRs, regardless of their size.

Previous studies showed that the thermal conductivity (TC) of Au NR solutions/nanofluids decreases with an increasing aspect ratio (AR = 2.1, 3.2, and 4.9) at room temperature, as demonstrated by Mohammadzadeh et al.[63] Additionally, Essajai et al.[64] showed through equilibrium molecular dynamics (EMD) simulations that Au NRs are more effective than Au NSs in enhancing the effective TC of nanofluids. However, our results indicate that incorporating either Au NSs or Au NRs of various sizes into the hydrogel matrix does not significantly alter the TC values as displayed in Fig. 7. This suggests that the gel structure may dominate the thermal transport properties, with negligible impact of the nanoparticle inclusions.

Computational simulations shown in Fig. 8(a) for 785 nm laser excitation and Fig. 8(b) for 808 nm excitation supported these findings, indicating that the PCE remained largely consistent across different nanoparticle types and laser wavelengths. Overall, our study emphasizes that factors such as nanoparticle morphology and the excitation wavelength do not play a substantial role in determining the efficiency of photothermal energy conversion in the system.

4. Conclusion

We investigated the photothermal heat transfer of CTAB-capped Au NR hydrogels and Au NS hydrogels under laser excitation at 785 and 808 nm, ensuring equalized optical extinction across all samples. Our findings indicate that, at the concentration used in this study, neither nanoparticle size, shape, nor excitation wavelength significantly impacts photothermal conversion efficiency (PCE), which remains within a consistently narrow range. Notably, Au NSs exhibit comparable or slightly higher PCE than Au NRs at specific excitation wavelengths, likely due to the alignment of their surface plasmon resonance with the laser excitation wavelength. These results suggest that factors beyond plasmonic resonance, such as the hydrogel matrix and heat dissipation mechanisms, play a dominant role in thermal response. This insight underscores the need for a holistic approach when designing nanoparticle-based photothermal systems for applications in biomedical therapies and energy conversion technologies.

Conflicts of interest

There are no conflicts to declare.

Data availability

The data supporting this article have been included as part of the ESI.†

Acknowledgements

References

1 M. Gorbunova, V. Apyari, S. Dmitrienko and Y. Zolotov, *TrAC*, 2020, **130**, 115974.

2 A. M. Alkilany, L. B. Thompson, S. P. Boulos, P. N. Sisco and C. J. Murphy, *Adv. Drug Delivery Rev.*, 2012, **64**, 190–199.

3 H. Hassan, P. Sharma, M. R. Hasan, S. Singh, D. Thakur and J. Narang, *Mater. Sci. Energy Technol.*, 2022, **5**, 375–390.

4 P. Kesharwani, R. Ma, L. Sang, M. A. S. Fatima, A. Sheikh, N. Gupta, Z. S. Chen and Y. Zhou, *Cancer*, 2023, **22**, 98.

5 X. Huang, S. Neretina and M. A. El-Sayed, *Adv. Mater.*, 2009, **21**, 4880–4910.

6 J. Stone, S. Jackson and D. Wright, *Nanobiotechnology*, 2011, **3**, 100.

7 H. Ma and M. Xue, *J. Mater. Chem. A*, 2021, **9**, 17569–17591.

8 H. Takahashi, Y. Niidome and S. Yamada, *Chem. Commun.*, 2005, 2247.

9 A. Zimmer, *Methods*, 1999, **18**, 286–295.

10 L. Tong, Y. Zhao, T. B. Huff, M. N. Hansen, A. Wei and J. X. Cheng, *Adv. Mater.*, 2007, **19**, 3136.

11 X. Huang, P. K. Jain, I. H. El-Sayed and M. A. El-Sayed, *Lasers Med. Sci.*, 2008, **23**, 217–228.

12 K. C. Black, N. D. Kirkpatrick, T. S. Troutman, L. Xu, J. Vagner, R. J. Gillies, J. K. Barton, U. Utzinger and M. Romanowski, *Mol. Imaging*, 2008, **7**, 50.

13 C. Loo, A. Lowery, N. Halas, J. West and R. Drezek, *Nano Lett.*, 2005, **5**, 709.

14 M. P. Melancon, W. Lu, Z. Yang, R. Zhang, J. Z. Cheng, A. M. Elliot, J. Stafford, T. Zhang and J. Li, *Mol. Cancer Ther.*, 2008, **7**, 1730.

15 Y. F. Huang, H. T. Chang and W. Tan, *Anal. Chem.*, 2008, **80**, 567.

16 A. Taheri, M. U. Khandaker, F. Moradi and D. A. Bradley, *Phys. Med. Biol.*, 2024, **69**, 045029.

17 I. M. N. Hamdan, I. A. Tekko and S. Bell, *Eur. J. Pharm. Biopharm.*, 2022, **179**, 105.

18 M. Ghafarkhani, C. B. Avci, R. Rahbarghazi, A. Karimi, M. Sadeghizadeh, A. Zarebkohan and F. Bani, *Sci. Rep.*, 2021, **11**, 23984.

19 T. B. Huff, L. Tong, Y. Zhao, M. N. Hansen, J. X. Cheng and A. Wei, *Nanomedicine*, 2007, **2**, 125.

20 Z. Qin, Y. Wang, J. Randrianalisoa, V. Raeesi, W. C. W. Chan, W. Lipinski and J. C. Bischof, *Sci. Rep.*, 2016, **6**, 29836.

21 L. Qiu, N. Zhu, Y. Feng, E. E. Michaelides, G. Żyła, D. Jing, X. Zhang, P. M. Norris, C. N. Markides and O. A. Mahian, *Phys. Rep.*, 2020, **843**, 1–81.

22 P. M. R. Pallavicini, G. Chirico and A. Taglietti, *Chem. – Eur. J.*, 2021, **27**, 15361–15374.

23 M. L. Taylor, R. E. Wilson, K. D. Amrhein and X. Huang, *Bioengineering*, 2022, **9**, 200.

24 S. Liao, W. Yue, S. Cai, Q. Tang, W. Lu, L. Huang, T. Qi and J. Liao, *Front. Chem.*, 2021, **12**, 664123.

25 R. Gans, Über die Form ultramikroskopischer Silberteilchen, *Ann. Phys.*, 1915, **352**, 270.

26 R. Ren, B. Xiong and J. Zhu, *Chem. – Eur. J.*, 2024, **30**, e202400851.

27 P. M. R. Paulo, P. Zijlstra, M. Orrit, E. Garcia-Fernandez, T. C. S. Pace, A. S. Viana and S. M. B. Costa, *Langmuir*, 2017, **33**, 6503.

28 C. L. Didychuk, P. Ephrat, A. Chamson-Reig, S. L. Jacques and J. J. L. Carson, *Nanotechnology*, 2009, **20**, 195102.

29 Z. S. Mbalaha, D. J. S. Birch and Y. Chen, *IET Nanobiotechnol.*, 2023, **17**, 103.

30 L. Arellano-Galindo, E. Villar-Alvarez, A. Varela, V. Figueroa, J. Fernandez-Vega, A. Cambón, G. Prieto, S. Barbosa and P. Taboada, *Int. J. Mol. Sci.*, 2022, **23**, 13109.

31 C. I. Won, A. Sahu, Y. H. Kim and G. Tae, *Ann. Biomed. Eng.*, 2012, **40**, 534–546.

32 J. Domingo-Diez, L. Souiade, V. Manzaneda-González, M. Sánchez-Díez, D. Megias, A. Guerrero-Martínez, C. Ramírez-Castillejo, J. Serrano-Olmedo and M. Ramos-Gómez, *Int. J. Mol. Sci.*, 2023, **24**, 13306.

33 W. Zhou, Y. Yao, H. Qin, X. Xing, Z. Li, M. Ouyang and H. Fan, *Int. J. Mol. Sci.*, 2024, **25**, 2018.

34 A. T. Diallo, M. Tlemcani, M. Khan, J. Spadavecchia and N. Djaker, *Part. Part. Syst. Charact.*, 2020, **37**, 2000255.

35 D. L. Amarasekara, C. S. Kariyawasam, M. A. Hejny, V. B. Torgall, T. A. Werfel and N. C. Fitzkee, *ACS Appl. Mater. Interfaces*, 2024, **16**, 4321–4332.

36 M. S. Rashwan, A. M. Al-Sheikh, H. Baskaran and C. Burda, Plasmonic Enhancement of Photothermal Conversion Efficiency in Gold-Nanoparticle Hydrogels, *ChemNanoMat*, 2025, e202400636.

37 V. K. Pustovalov, *Nanotechnol. Precis. Eng.*, 2024, **7**, 015001.

38 N. M. Figueiredo, R. Serra and A. Cavaleiro, *Nanomaterials*, 2021, **11**, 1592.

39 Y. Chen, K. Wang, J. Huang, X. Li and Y. Rui, *Curr. Res. Biotechnol.*, 2024, **8**, 100234.

40 D. M. Alshangiti, M. M. Ghobashy, H. A. Alqahtani, T. K. El-Damhougy and M. Madani, *RSC Adv.*, 2023, **13**, 32223–32265.

41 D. E. Hudson, D. O. Hudson, J. M. Wininger and B. D. Richardson, *Photomed. Laser Surg.*, 2013, **31**, 163–168.

42 J. Wang, Q. Duan, M. Yang, B. Zhang, L. Guo, P. Li, W. Zhang and S. Sang, *Beilstein J. Nanotechnol.*, 2021, **12**, 462–472.

43 S. R. Tsai and M. R. Hamblin, *J. Photochem. Photobiol., B*, 2017, **170**, 197–207.

44 M. Nour, O. Hamdy, A. H. Faid, E. A. Eltayeb and A. A. Zaky, *Lasers Med. Sci.*, 2022, **37**, 3551–3560.

45 W. J. Kennedy, S. Izor, B. D. Anderson, G. Frank, V. Varshney and G. Ehlert, *ACS Appl. Mater. Interfaces*, 2018, **10**, 43865–43873.

46 W. Yang, H. Liang, S. Ma, D. Wang and J. Huang, *SM&T*, 2019, **22**, e00109.

47 M. S. Rashwan, H. Baskaran and C. Burda, *Adv. Funct. Mater.*, 2024, **34**, 2309440.

48 H. Hameed, S. Faheem, A. C. Paiva-Santos, H. S. Sarwar and M. A. Jamshaid, *AAPS PharmSciTech*, 2024, **25**, 64.

49 F. Pervin and W. W. Chen, *J. Biomech.*, 2009, **42**, 731–735.

50 A. Irastorza-Lorenzo, D. Sánchez-Porras, O. Ortiz-Arrabal, M. J. de Frutos, E. Esteban, J. Fernández, A. Janer, A. Campos, F. Campos and M. Alaminos, *Int. J. Mol. Sci.*, 2021, **22**, 1923.

51 M. A. Salati, J. Khazai, A. M. Tahmuri, A. Samadi, A. Taghizadeh, M. Taghizadeh, P. Zarrintaj, J. D. Ramsey, S. Habibzadeh and F. Seidi, *Polymers*, 2020, **12**, 1150.

52 T. A. Vilgis, *Curr. Opin. Food Sci.*, 2015, **3**, 71–84.

53 M. Khodadadi Yazdi, A. Taghizadeh, M. Taghizadeh, F. J. Stadler, M. Farokhi, F. Mottaghitalab, P. Zarrintaj, J. D. Ramsey, F. Seidi and M. R. Saeb, *J. Control Release*, 2020, **326**, 523–543.

54 J. Turkevich and J. Hillier, *Anal. Chem.*, 1949, **21**, 475–485.

55 X. Ye, C. Zheng, J. Chen, Y. Gao and C. B. Murray, *Nano Lett.*, 2013, **13**, 765–771.

56 N. B. Milbrandt, Y. H. Tsai, K. Cui, C. S. Ngompe Massado, H. Jung, A. Visperas, A. Klika, N. Piuzzi, C. A. Higuera-Rueda and A. C. S. Samia, *ACS Appl. Bio Mater.*, 2023, **6**, 1231–1241.

57 B. Nikoobakht and M. A. El-Sayed, *Mater. Chem.*, 2003, **15**, 1957–1962.

58 M. Tako, Y. Tamaki, T. Teruya and Y. Takeda, *Food Nutr. Sci.*, 2014, **5**, 280–291.

59 M. Fan, Y. Han, S. Gao, H. Yan, L. Cao, Z. Li, X. J. Liang and J. Zhang, *Theranostics*, 2020, **10**, 4944–4957.

60 N. Soto-Reyes, A. L. Temis-Pérez, A. López-Malo, R. Rojas-Laguna and M. E. Sosa-Morales, *J. Food Sci.*, 2015, **80**, E1021–E1025.

61 R. L. Hamilton and O. K. Crosser, *J. Ind. Eng. Chem.*, 1962, **1**, 187–191.

62 S. Unser, I. Bruzas, J. He and L. Sagle, *Sensors*, 2015, **15**, 15684–15716.

63 M. Mohammadzadeh, M. Ashjari and D. Zare, *Tech. Sci.*, 2019, **22**, 119–133.

64 R. Essajai, A. Mzerd, N. Hassanain and M. Qjani, *J. Mol. Liq.*, 2019, **293**, 111494.